Available online at www.sciencedirect.com
ScienceDirect
Trans. Nonferrous Met. Soc. China 34(2024) 2629−2644
Transactions of Nonferrous Metals Society of China
www.tnmsc.cn

Vermiform Ni@CNT derived from one-pot calcination of Ni-MOF precursor for improving hydrogen storage of MgH_2

Zi-yin DAI[1,#], Bing ZHANG[1,#], Hideo KIMURA[1], Li-rong XIAO[1], Rong-han LIU[1], Cui NI[1], Chuan-xin HOU[1], Xue-qin SUN[1], Yu-ping ZHANG[1], Xiao-yang YANG[1], Rong-hai YU[2], Wei DU[1], Xiu-bo XIE[1]

1. School of Environmental and Material Engineering, Yantai University, Yantai 264005, China;
2. Key Laboratory of Aerospace Materials and Performance, Ministry of Education, School of Materials Science and Engineering, Beihang University, Beijing 100191, China

Received 30 December 2022; accepted 6 July 2023

Abstract: The Ni-coated carbon nanotubes (Ni@CNT) composite was synthesized by the facile "filtration + calcination" of Ni-based metal−organic framework (MOF) precursor and the obtained composite was used as a catalyst for MgH_2. MgH_2 was mixed evenly with different amounts of Ni@CNT (2.5, 5.0 and 7.5, wt.%) through ball milling. The MgH_2−5wt.%Ni@CNT can absorb 5.2 wt.% H_2 at 423 K in 200 s and release about 3.75 wt.% H_2 at 573 K in 1000 s. And its dehydrogenation and rehydrogenation activation energies are reduced to 87.63 and 45.28 kJ/mol (H_2). The in-situ generated Mg_2Ni/Mg_2NiH_4 exhibits a good catalytic effect due to the provided more diffusion channels that can be used as "hydrogen pump". And the presence of carbon nanotubes improves the properties of MgH_2 to some extent.
Key words: Mg-based hydrogen storage material; activation energy; Ni-loaded carbon nanotubes; catalyst; mechanism

1 Introduction

The excessive use of fossil fuels in recent years has provoked increasing global concern. Fossil energy is nonrenewable and its consumption leads to the emission of carbon dioxide, which exacerbates the greenhouse effect, contributing to the melting of Arctic glaciers and elevated sea levels [1]. From this viewpoint, seeking novel energy consumption solutions in an effort to resolve the aforementioned challenges faced by the exploitation of fossil energy is urgent. The current novel energy sources include biomass, wind, solar, and hydrogen energies [2]. These energy sources are clean, renewable, and do not cause secondary environmental pollution. Among these sources of energy, nuclear power produces nuclear waste, and wind, solar, and tidal energies are time sensitive. Given the constraints of weather and time, these alternative sources of energy cannot possibly replace fossil energy within the foreseeable future [3]. Comparatively, hydrogen energy, with its clean and efficient applications, stands out as a unique alternative energy source [4,5]. Since the 1970s, countries all over the world have attempted to conduct research on hydrogen energy. Technologies for hydrogen production, storage, transportation, and application have evolved with time and have become the focus of research in the 21st century [6,7].

Effective and secure hydrogen storage is critical for increasing hydrogen energy and achieving carbon peaking and carbon neutrality. In

Zi-yin DAI and Bing ZHANG contributed to this work equally
Corresponding author: Wei DU, Tel: +86-15253559837, E-mail: duwei@ytu.edu.cn;
Xiu-bo XIE, Tel: +86-15054555676, E-mail: xiuboxie@ytu.edu.cn
DOI: 10.1016/S1003-6326(24)66565-9

recent years, high-pressure gaseous, low-temperature liquid, and solid-state hydrogen storage have become subjects of extensive research [8]. Among these types, solid-state hydrogen storage materials exhibit superior safety performance, exceptional storage capacity per unit volume, and small footprint [9]. Mg-based hydrogen storage materials stand out among several solid-state hydrogen storage materials due to their advantages of abundant earth storage capacity, low material cost, and excellent hydrogen storage capacity (7.6 wt.%) [10]. However, the prospects of MgH_2 as an onboard energy source are limited by their slow kinetics and high operating temperatures [11].

Current studies have been focused on enhancing the hydrogen storage properties of MgH_2 through nanoconfinement, alloying, and catalyst addition [12−14]. Transition group metals, which serve as the predominantly-employed catalysts (particularly Ni-based catalysts), exhibit excellent catalytic effects. Pure Ni nanoparticles (NPs) can store H_2 via physical adsorption after treatment. ZHOU et al [15] prepared nonporous Ni with a specific surface area of 120.5 m^2/g using SiO_2 aerogel as the template. Special nonporous Ni can store 0.45 wt.% H_2 under 4.5 MPa H_2 at ambient temperatures. The hydrogen storage capacity of physical adsorption was considerably lower than that of metal hydride. Similarly, studies involving Ni as catalysts have shown that Ni can enhance the hydrogen storage properties of MgH_2. YANG et al [16] used wet chemical ball milling to create flaky Ni NPs. According to experimental results, onset hydrogen release temperature was reduced to 180 °C, and the hydrogen absorption capacity can reach 4.6 wt.% in 20 min at 125 °C. The in-situ synthesized Mg_2Ni/Mg_2NiH_4 can act as a "hydrogen pump" to accelerate hydrogen diffusion. However, the Ni particles agglomerated with each other during the experimental cycle.

Therefore, a method to prevent Ni particles from agglomeration was required to increase the cycle performance. GAO et al [17] first added a novel Ni-based metal−organic framework (Ni-MOF) to MgH_2, and the results demonstrated the excellent catalytic activity of MOFs. The MgH_2−5wt.%Ni−MOF can absorb about 5.7 wt.% H_2 at 150 °C and release 6.4 wt.% H_2 at 300 °C. The remarkable performance was attributed to the synergistic catalytic action of Mg_2Ni/Mg_2NiH_4, MgO, and amorphous C. These results demonstrated that the introduction of carbon materials can promote catalytic performance of Ni-based catalyst. HUANG et al [18] synthesized Ni NPs coated with carbon (Ni/C) via pyrolysis of MOFs. The MgH_2−6wt.%Ni/C can release 6.1 wt.% H_2 at 250 °C and can uptake 5.0 wt.% H_2 at 100 °C within 20 s. Compared with pure Ni catalysts, the doped carbon can effectively inhibit the aggregation of catalysts by attaching to the surface of catalyst particles. LAN et al [19] reported that the Ni@reduced graphene oxide (rGO) catalyst was more effective than pure Ni and pure graphene addition. YAO et al [20] successfully dispersed Ni NPs uniformly on rGO. The results revealed that the initial hydrogen release temperature of MgH_2−10wt.%Ni_4@rGO_6 was reduced from 251 °C (pure MgH_2) to 190 °C. The rGO diffused Ni more evenly and enhanced the specific surface area of the catalyst. Carbon materials with two and three-dimensional structures exhibit a higher specific surface area than those with a shell structure. REYHANI et al [21] produced Ni via a hydrothermal reduction and employed a chemical technique to deposit Ni NPs onto carbon nanotubes (CNTs) to obtain a greater surface area and distribute Ni NPs. By combining Ni with CNTs, the composite successfully achieved a high specific surface area. However, the Ni particles were exposed on the surface of CNTs, which may have led to unsatisfactory agglomeration. Several investigations have revealed that Ni particles agglomerate during cycling, which decreases the effectiveness of catalysts. Previous studies implied that CNT structures can be formed under the catalytic effect of Ni. SUN et al [22] grew CNT structures on the graphene surface by direct pyrolytic synthesis. Ni NPs wrapped in carbon films were uniformly dispersed on the CNT chamber and graphene surfaces. This method limited the formation of agglomerates. However, this process used graphene as a carbon source to generate CNTs. Some Ni particles remained exposed on the surface of graphene, which weakened the catalytic effect. Under this condition, optimization of the preparation process involved the introduction of carbon materials. This process is the best available method to prevent Ni particles from agglomerating, increasing the specific surface area of composites.

In this work, the preparation process of

metallic and carbon materials was improved. Compared with the previous complex synthesis approaches, Ni@CNT composite was synthesized using a simple "filtration + calcination" method. In this process, Ni-MOF precursor was synthesized by filtration, and vermiform CNTs were catalyzed by calcination in the presence of Ni. CNT provided some degree of protection to the metallic material and curbed the oxidation. The Ni@CNT composite synthesized using this simple method may provide new ideas for the synthesis of future transition-group metal composite carbon materials.

2 Experimental

2.1 Materials

N,N-dimethylformamide (DMF) was got from Sinopharm Chemical Reagent Co. Ltd. (China). Nickel acetate tetrahydrate ($Ni(CH_3COO)_2·4H_2O$), p-phthalic acid ($C_8H_6O_4$) and triethylamine ($C_6H_{15}N$) were purchased from Macklin Reagent. All reagents were used according to the received standard.

2.2 Synthesis of MgH_2/Ni@CNT

2.2.1 Synthesis of Ni@CNT

The Ni@CNT composite was first synthesized by the sol−gel method. The experimental process is shown in Fig. 1. Firstly, 11.25 mmol $Ni(CH_3COO)_2·4H_2O$ was dissolved in 125 mL DMF and magnetically stirred for 0.5 h (Liquid A). Secondly, 9 mmol $C_8H_6O_4$ (terephthalic acid) and 2.125 mL $C_6H_{15}N$ (triethylamine) solution were magnetically stirred in 100 mL DMF solution for 0.5 h (Liquid B). Then, Liquid B was slowly poured into Liquid A and stirred for 1 h. Following stirring, the precursor gel was vacuum filtered and washed with DMF. The sample was calcined in a tube furnace using argon gas for 10 h in the final step of the experiment. The heating rate is 5 °C/min. The powder obtained after natural cooling can be used without further treatment.

2.2.2 Synthesis of MgH_2−$x$wt.%Ni@CNT

In this experiment, Ni@CNT catalyst was added into MgH_2 by high-energy ball milling. 2.5, 5 or 7.5 wt.% catalyst was added. The total mass of the sample was 2 g, and the mass of the stainless-steel ball was 60 g. This operation had to be run at 450 r/min for 12 h, with 15 min breaks every 45 min. At the end of the mill, samples were collected in a glove box filled with protective gas.

2.3 Characterizations

X-ray diffraction (XRD, Shimadzu XRD−7000) with Cu K_α radiation was used to determine the crystal structure. The scan speed was 6 (°)/min, and 2θ ranged from 20° to 90°. The morphology and microstructure of the samples were determined by scanning electron microscope (SEM, JEOLJSM−7610F, Japan) and transmission electron microscope (TEM, JEOLJSM−2100f, Japan). The degree of graphitization was performed by Raman spectroscopy (Raman, Olympus, Lmplfln5). The X-ray photoelectron spectroscopy (XPS, Thermo Scientific K-Alpha, USA) was used to conduct the compositional analysis and elemental analysis. N_2 adsorption and desorption curves were measured by a surface analyzer, and specific surface area and pore size distributions were obtained by Brunauer−Emett−Teller (BET) method and Barrett−Joyner−Halenda (BJH) method.

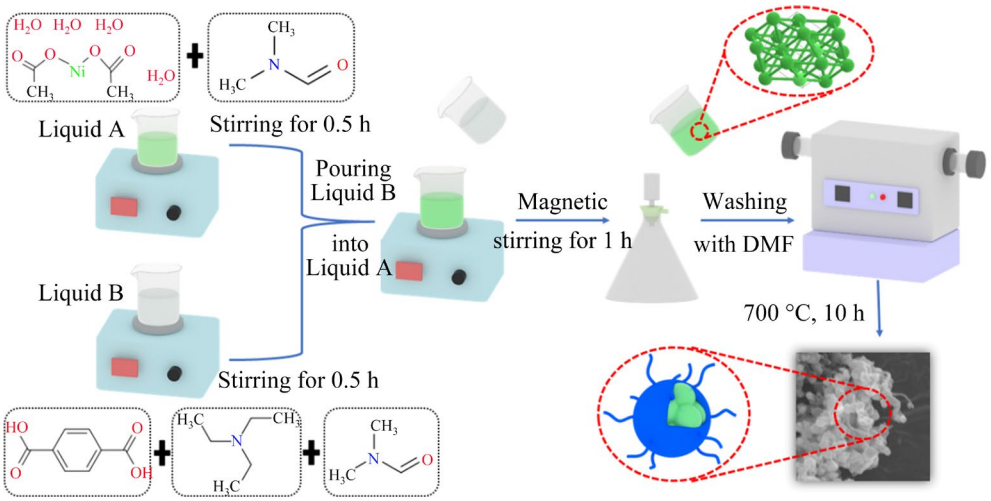

Fig. 1 Schematic diagram of preparation of Ni@CNT

The kinetics curves of MgH_2−Ni@CNT composites were measured by heating them to test temperature under the condition of complete dehydrogenation. The hydrogen absorption and dehydrogenation were carried out under a pressure of 5.0 MPa and −0.0001 MPa, respectively. The pressure−composition−temperature (PCT) curves were tested at 673, 648 and 623 K to calculate the thermodynamic performance. The cyclic stability test was conducted at a stable temperature of 673 K. The dehydrogenation pressure is −0.0001 MPa and the hydrogen absorption pressure is 5.0 MPa.

3 Results and discussion

3.1 Characterization of prepared Ni@CNT

The XRD pattern (Fig. 2(a)) was used to determine the phase composition of the Ni@CNT composite. The diffraction peaks detected at 2θ=44.5°, 51.8°, and 76.4° are attributed to the (111), (200), and (220) crystal planes of cubic Ni (FCC, PDF# 04-0850), respectively. The peak centering at 2θ=26° corresponds to the graphite structure of CNT, which is different from the amorphous carbon with a broad diffraction peak. As a result, it is believed that the presence of Ni in this work serves as a catalyst to facilitate the catalysis of CNT. Figure 2(b) shows the Raman spectrum with prominent D and G peaks at 1348.5 and 1568.2 cm^{-1}, respectively. The ratio of I_D/I_G can be used to determine the graphitization degree of the composites. The calculated value of I_D/I_G is 0.91, which proves the presence of several defects in the carbon composites. This result further proves the existence of amorphous carbon. This feature facilitates the nucleation of Mg/MgH_2 in the hydrogen absorption and desorption cycles [23]. ZHOU et al [24] reported that hydrogen absorption may be related to defects in carbon materials. The maintenance of defects may benefit hydrogen transportation during cycling. Typical type-IV N_2 absorption–desorption isotherms can be determined and the curves are shown in Fig. 2(c). When P/P_0 is in the range of 0.5−1.0, the adsorption amount of N_2 is less than desorption amount, indicating that Ni@CNT displays mesoporous characteristics. The

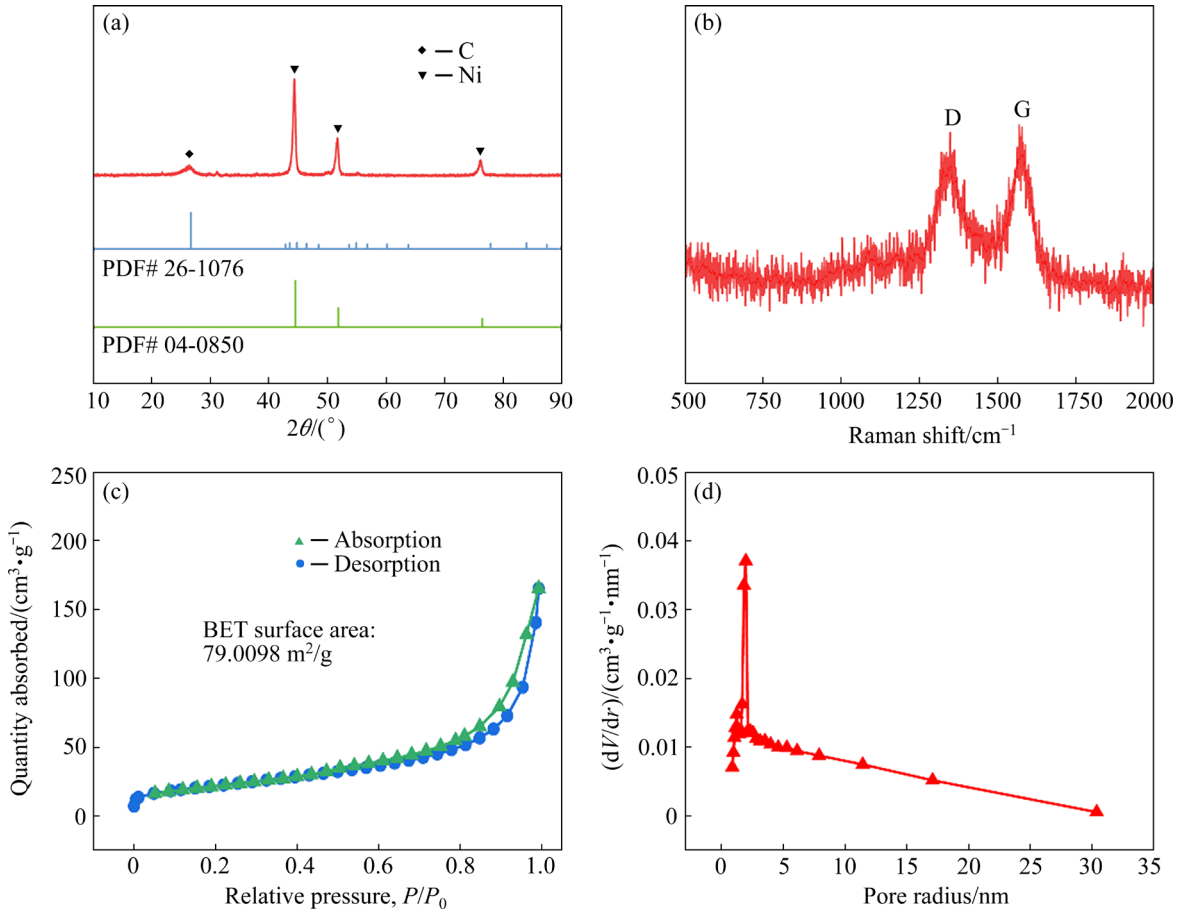

Fig. 2 XRD pattern (a), Raman spectrum (b), nitrogen absorption−desorption isotherms (c) and pore-size distribution (d) of Ni@CNT composite

BET surface area of the Ni@CNT is determined to be 79.01 m^2/g (Fig. 2(c)), which is substantially greater than that of the Ni/C composite obtained in previous work [22]; this finding demonstrates that the CNTs lead to an increase in the specific surface area. Figure 2(d) shows the pore size distribution curve and a porous structure of 2−5 nm, which are primarily attributed to the generation of CNTs. The high specific surface area can cause the even dispersion of the catalyst, thus enhancing the catalytic effect. The surface chemical compositions and valence state of Ni@CNT are revealed by XPS measurements. Figure 3(a) displays the full XPS spectrum of this catalyst, and the peaks corresponding to C 1s and Ni 2p are easily identifiable. As shown in Fig. 3(b), Ni 2p spectrum exhibits the core energy levels of Ni $2p_{3/2}$ and Ni $2p_{1/2}$: the peaks at 853.48 and 870.48 eV are typically characterized as Ni^0, and peaks at 855.08/871.68 and 856.38/873.48 eV are attributed to Ni^{2+} and Ni^{3+} [25], respectively, and caused by the inevitable oxidation in the sample transfer and test process. Moreover, by comparing the peak positions, the peaks located at 861.70 and 879.70 eV correspond to the satellite peaks of Ni^{2+} and Ni^{3+}, respectively [26]. As displayed in Fig. 3(c), the binding energy peaks centering at 284.8, 285.4, and 290.3 eV in the C 1s spectrum of Ni@CNT belong to the groups of C—C, Ni—C, and C═O bonds, respectively [27]. The results demonstrated the successful synthesis of the Ni@CNT composite.

Figure 4 displays the microstructures of the Ni@CNT composite. The microstructures in Figs. 4(a, b) confirm that Ni@CNT NPs are produced by “filtration + calcination” approach. Ni particles with a size of 100 nm agglomerate, and CNTs extend to the surface at the edge of the particles, exhibiting a vermiform-like morphology. Figures 4(c, d) display the elemental mappings of Ni@CNT NPs. C and Ni are distributed evenly, and Ni particles can be observed in Fig. 4(d). However, C content is lower in the Ni-rich area, indicating that the CNTs may cover around the Ni NPs.

The microstructures of Ni@CNT composite were analyzed in detail by TEM, and the results are shown in Fig. 5. Figure 5(a) shows the dense distribution of nanotube structures surrounding the spherical particles, similar to the findings of SEM images. To determine the phase composition of nanotubes, the lattice stripes were obtained from the

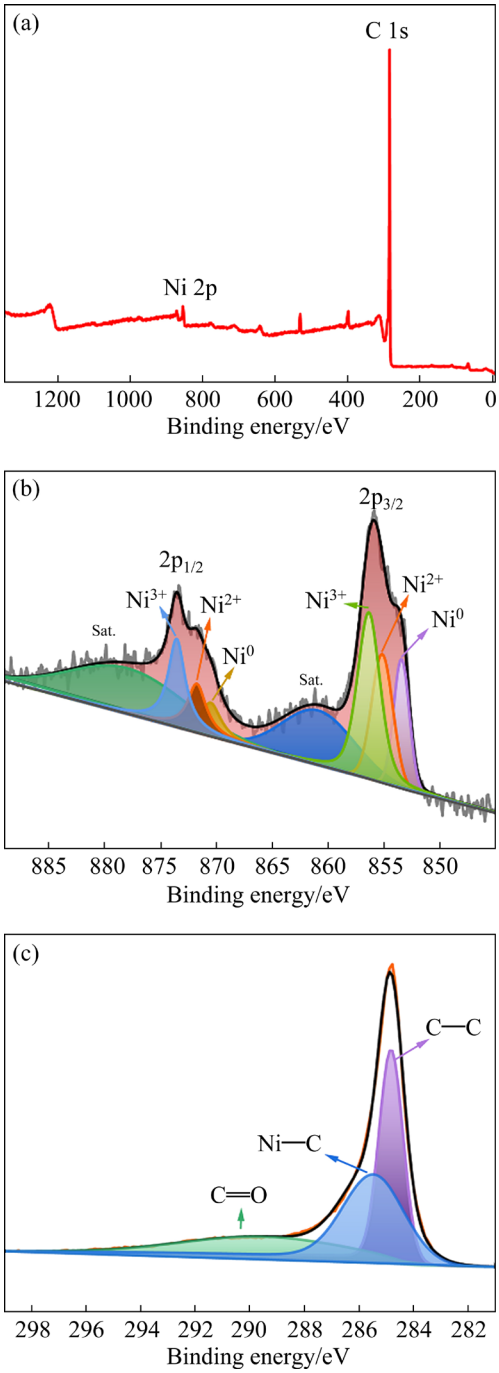

Fig. 3 XPS spectra of Ni@CNT: (a) Survey spectrum; (b) High-resolution spectrum of Ni 2p; (c) High-resolution spectrum of C 1s

high-resolution TEM images (Fig. 5(b)). The lattice spacing of the nanotubes grown at the edge of particles is 0.3500 nm, corresponding to the C (003) crystal plane (the standard crystal plane spacing is 0.3480 nm), indicating the existence of CNTs. After lattice measurement in the NPs region (Fig. 5(c)), the plane spacing of the inner black region in Fig. 5(d) is measured to be 0.2300 nm, which

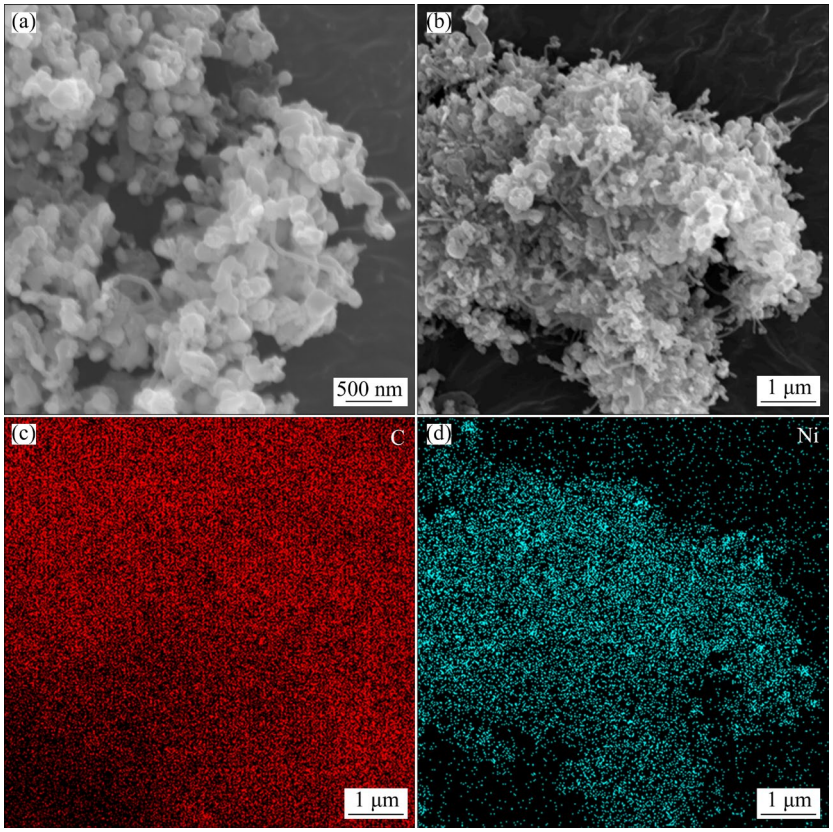

Fig. 4 SEM images (a, b) and elemental mappings (c, d) of Ni@CNT

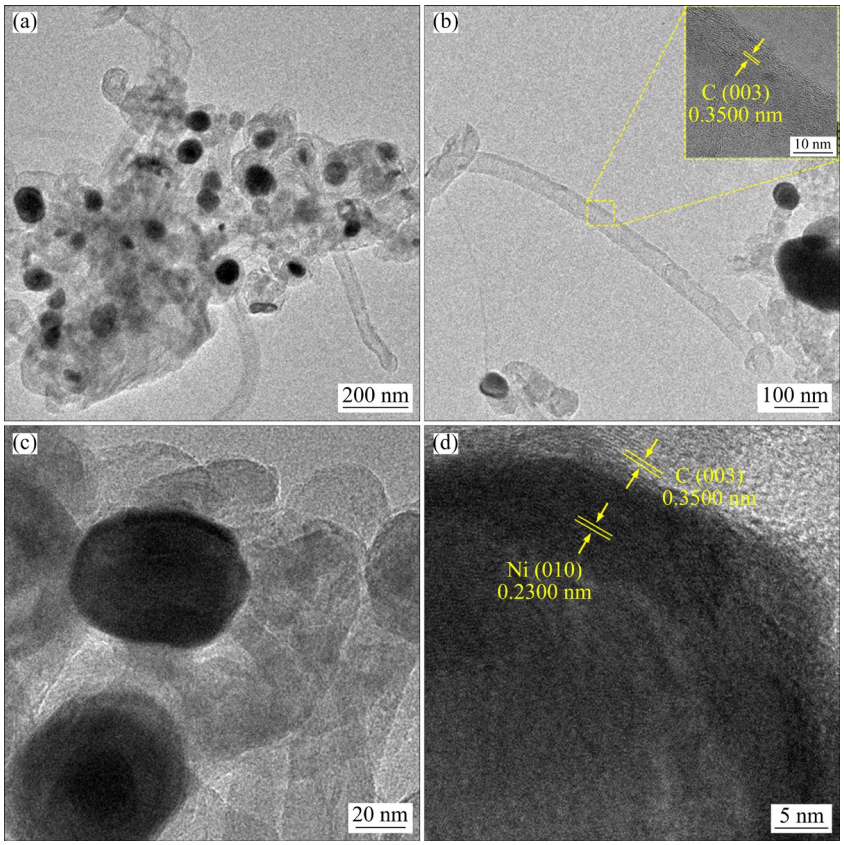

Fig. 5 TEM image of Ni@CNT (a), TEM and HRTEM images of CNT (b), and TEM (c) and HRTEM (d) images of core area

coincides with the standard spacing of 0.2302 nm in the Ni (010) plane. The lattice spacing of the outer structure is 0.3500 nm, corresponding to the (003) plane of C with a standard spacing of 0.3480 nm. This phase reveals that when metals, such as Ni, Fe [28], and Co [29], are present in carbon source, CNT structures are produced at high temperatures; this phenomenon is consistent with the results obtained in this work. The above results demonstrate that Ni@CNT composite is successfully synthesized by the "filtration + calcination" method. The CNTs are encapsulated in the surface layer of the Ni particles and grow outward under the catalytic effect of Ni particles.

3.2 Characterization of MgH_2–*x*wt.%Ni@CNT

Figure 6 displays the XRD patterns of MgH_2–Ni@CNT in different conditions: ball milled, dehydrogenated, and rehydrogenated. As presented in Fig. 6(a), the weak diffraction peaks at around 2θ=44° and 76° belong to Ni (PDF# 04-0850). The diffraction peaks of Ni become more apparent with the increase in the content of Ni@CNT in the composite. The dominating diffraction peaks at 2θ=27°, 36°, and 54° can be ascribed to MgH_2 (PDF# 12-0697). These findings demonstrate that no reactions occur in the ball-milling process. Moreover, a diffraction peak centered at 2θ=43° corresponds to MgO, and the same diffraction peak appears in Figs. 6(b, c). The appearance of MgO can be attributed to oxidation, which inevitably occurs due to its contact with air during the testing process [30]. Figure 6(b) indicates that the peaks of dehydrogenated MgH_2–Ni@CNT composite are indexed to Mg (PDF# 35-0821) and Mg_2Ni (PDF# 35-1225). The above results indicate that during hydrogen release, Ni reacts with MgH_2 and is transferred in-situ to Mg_2Ni and H_2. As shown in Fig. 6(c), the diffraction peaks at 2θ=24°, 39°, and 62° should be identified as Mg_2NiH_4 (PDF# 37-1414). The phase transition between MgH_2 and Ni during the absorption–desorption processes can be elaborated as follows:

$$2MgH_2+Ni=Mg_2Ni+2H_2=Mg_2NiH_4 \quad (1)$$

Furthermore, these results confirm the existence of reversible phase transitions between Mg/MgH_2 and Mg_2Ni/Mg_2NiH_4.

The isothermal hydrogenation–dehydrogenation curves of the MgH_2–Ni@CNT composites were recorded at different temperatures to further determine the catalytic effect of Ni@CNT. As displayed in Figs. 7(a, c, e), all samples display remarkable rapid hydrogen absorption kinetics above 423 K. Ni@CNT can enhance the hydrogen absorption rate of MgH_2. By comparison, the hydrogenation rate and the capacity of MgH_2–5wt.%Ni@CNT are optimal at 423 K. This material

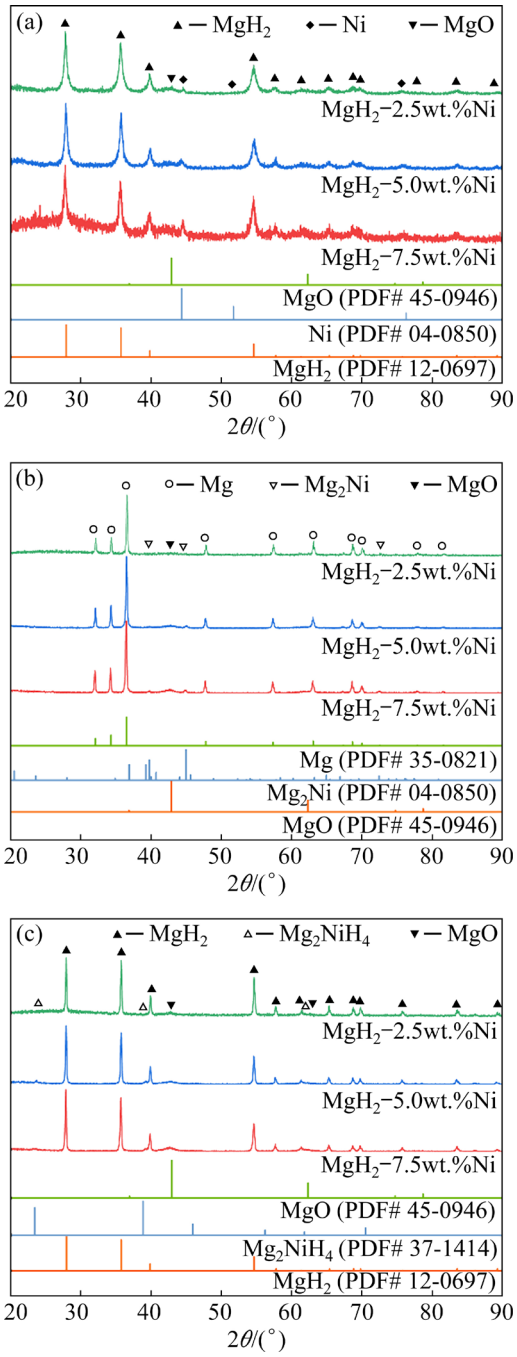

Fig. 6 XRD patterns of MgH_2–Ni@CNT in different conditions: (a) Ball-milled; (b) Dehydrogenated; (c) Rehydrogenated

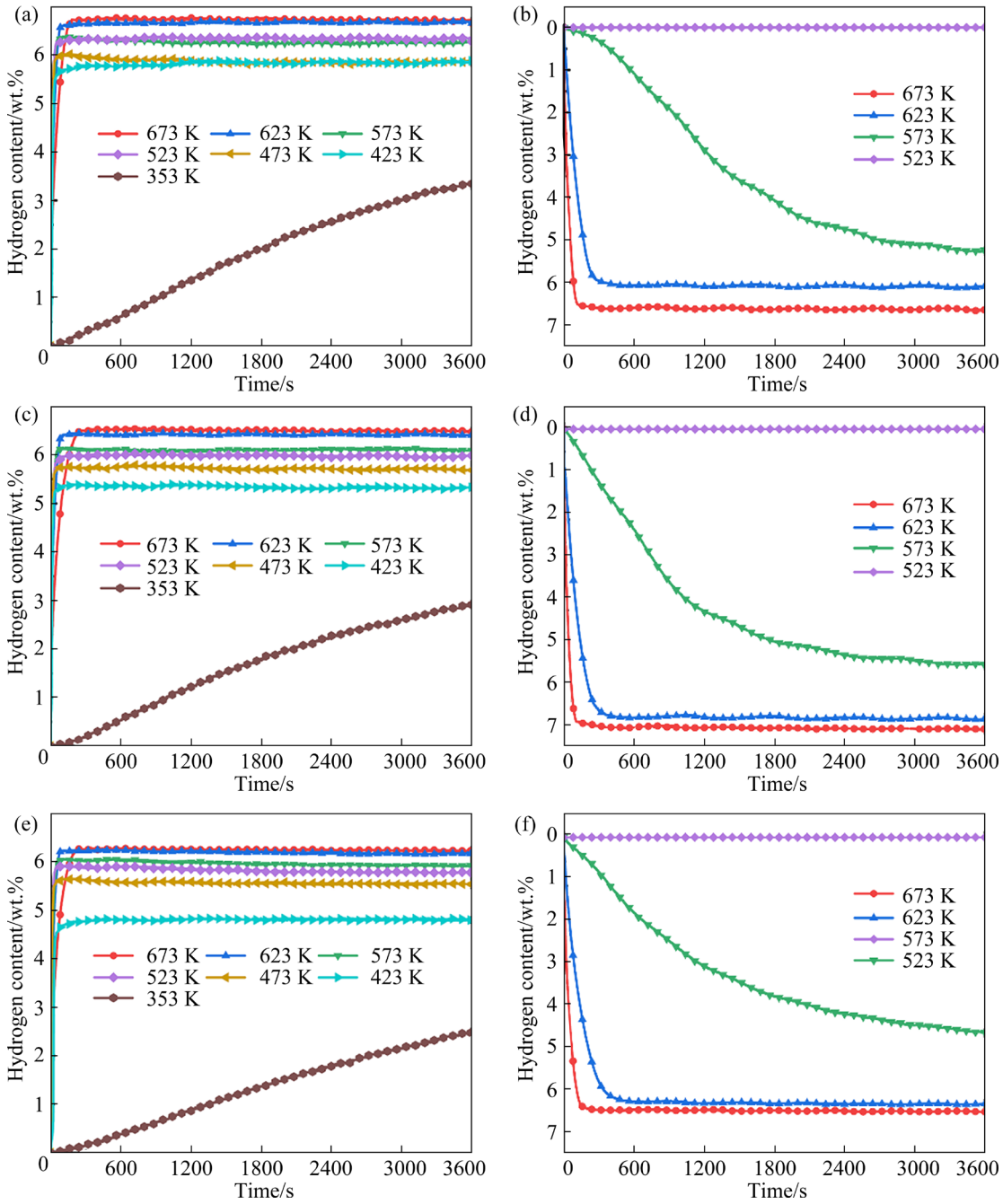

Fig. 7 Isothermal hydrogenation (a, c, e) and dehydrogenation (b, d, f) curves for composites: (a, b) MgH_2−2.5wt.%Ni@CNT; (c, d) MgH_2−5wt.%Ni@CNT; (e, f) MgH_2−7.5wt.%Ni@CNT

can absorb at least 5.2 wt.% H_2 at 423 K in 200 s (Fig. 7(c)). MgH_2−2.5wt.%Ni@CNT and MgH_2−7.5wt.%Ni@CNT composites can uptake 4.7 wt.% and 4.1 wt.% H_2, respectively. Figures 7(b, d, f) show the hydrogen release properties of the composites. In comparison with other samples, 5 wt.% Ni@CNT exhibits the best catalytic effect on kinetics. As shown in Fig. 7(d), MgH_2−5wt.%Ni@CNT can release 3.75 wt.% H_2 at 573 K in 1000 s. However, MgH_2−2.5wt.%Ni@CNT and MgH_2−7.5wt.%Ni@CNT can only release 2.3 and 2.25 wt.% hydrogen under the same conditions, respectively. These performances demonstrate that the rates of hydrogenation and dehydrogenation are enhanced with the increase in temperature. The Mg–Ni/TCN composite prepared by LI et al [31] can only release and uptake 1.01 and 3.5 wt.% H_2 at 573 and 423 K in 500 s, respectively. The sample added with 5 wt.% Ni@CNT can absorb 5.2 wt.% H_2 and desorb 1.85 wt.% H_2 in this work. AN and DENG [32] synthesized Ni@C, and 4 wt.% Ni@C exhibits the best catalytic properties. The composite

can absorb approximately 5 wt.% H_2 in 500 s at 543 K; in contrast, the composite in this work can absorb more hydrogen. For a more visual comparison, Fig. 8(e) shows the hydrogen release capacity of the three samples at different temperatures for 10 min. The experimental results demonstrate that the addition of 5 wt.% Ni@CNT to the composite allows it to achieve optimal hydrogen release properties, especially at low temperatures. These results reveal that 5.0 wt.% Ni@CNT maximizes the performance of MgH_2.

To demonstrably explain the influence of Ni@CNT additive on dehydrogenation kinetics, the activation energy (E_a) was calculated using the Johnson–Mehl–Avrami–Kolmo model, which is written in Eq. (2):

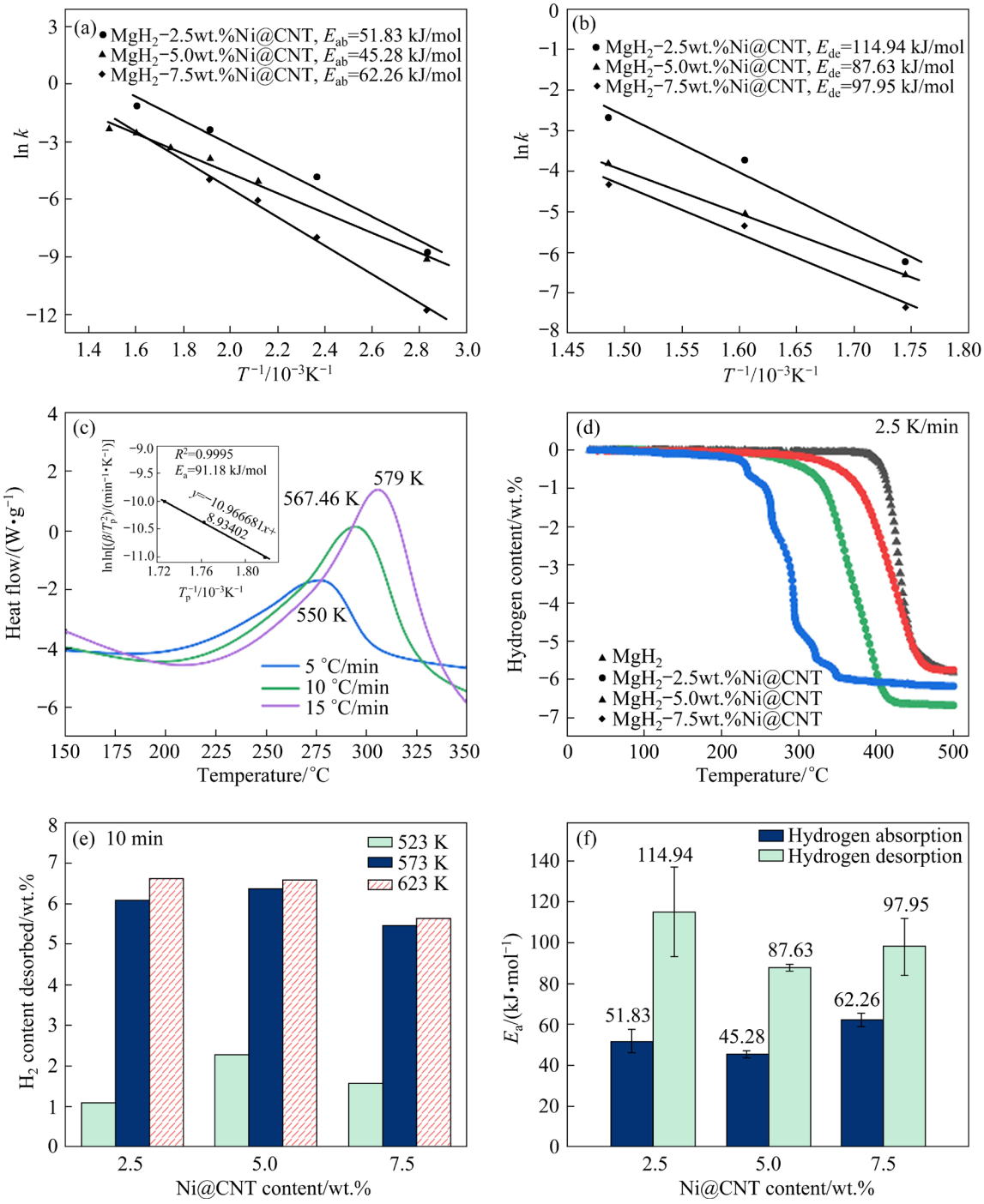

Fig. 8 Activation energy fitting diagrams for hydrogen absorption (a) and desorption (b); DSC plot of MgH_2−5wt.%Ni@CNT (c); Temperature programmed desorption (TPD) curves (d); Dehydrogenation capacity (e) and activation energy (f) of MgH_2−$x$wt.%Ni@CNT (x=2.5, 5.0, 7.5)

$$\ln[-\ln(1-\alpha)]=\eta\ln k+\eta\ln t \quad (2)$$

At time t, the conversion ratio of MgH_2 is α, k denotes the effective kinetic parameters, and η denotes the Avrami index. The lines of $\ln[-\ln(1-\alpha)]$ versus $\ln t$ can be drawn through the isothermal kinetics data at 353, 423, 473, 523, 573, 623, and 673 K, from which the values of η and $\ln k$ can be calculated (Figs. S1−S3 in Supplementary Information (SI)). Subsequently, the Arrhenius equation, which is shown in Eq. (3), can be used to calculate the activation energy (E_a):

$$\ln k=E_a/(RT)+\ln A \quad (3)$$

where A, R, and T represent a temperature-independent coefficient, the molar gas constant, and thermodynamic temperature, respectively. As shown in Fig. 8(a), the calculated hydrogenation E_a values of MgH_2−$x$wt.%Ni@CNT (x=2.5, 5.0, 7.5) composites are determined to be 51.83, 45.28, and 62.26 kJ/mol H_2, respectively. The dehydrogenation activation energies are 114.94, 87.63, and 97.95 kJ/mol H_2 (Fig. 8(b)). Figure 8(f) presents the comparison of E_a values. MgH_2−5wt.%Ni@CNT composite exhibits the lowest dehydrogenation E_a, indicating that it possesses the fastest kinetics. The value is notably lower than that of pure MgH_2 (155 kJ/mol H_2) [33]. AN and DENG [32] determined that the dehydrogenation E_a of MgH_2−4wt.%Ni@C was as high as 112 kJ/mol (H_2). DAN et al [34] reported that the ultrafine Ni NPs synthesized from the precursor Ni acetylacetonate via H_2 plasma reduction process exhibited a high dehydrogenation E_a value of 112.1 kJ/mol (H_2). Compared with the above studies, the sample doped with 5 wt.% Ni@CNT exhibits the lowest activation energy. To ensure the accuracy of calculations, the differential scanning calorimetry (DSC) curves of MgH_2−5wt.%Ni@CNT were determined (Fig. 8(c)). The value was calculated based on Kissinger's equation [35] (Eq. (4)):

$$\ln[\beta/T_p^2]=C-E_a/(RT_p) \quad (4)$$

where β, T_p, and C represent the heating rate, peak temperature, and a constant, respectively. DSC experiments were performed at heating rates of 5, 10, and 15 °C/min to calculate E_a (Fig. 8(c)). The DSC curves of MgH_2−5wt.%Ni@CNT reveal the presence of a primary endothermic peak on the curves above 520 K, which is primarily attributed to the dehydrogenation of Mg_2NiH_4 earlier in the process and the accelerated dehydrogenation of MgH_2 caused by the generation of Mg_2Ni. This phenomenon causes the DSC desorption peaks of MgH_2 and Mg_2NiH_4 to nearly overlap; thus, each curve exhibits an endothermic peak [36]. The E_{de} calculated from Kissinger's equation is 91.18 kJ/mol (H_2), which differs slightly from 87.63 kJ/mol (H_2) (Fig. 8(d)). Table 1 compares the hydrogen absorption–desorption activation energies and initial hydrogen release temperatures of the Mg complex system [37−40].

Figure 8(d) displays the curves obtained from the temperature programmed desorption (TPD) test; these findings were used to investigate the dehydrogenation properties of pure MgH_2 and MgH_2 with catalysts. Pure MgH_2 was processed through high-energy ball milling before use to ensure that the MgH_2 particle size was the same as that of the doped catalyst sample. The initial hydrogen emission temperatures of the composites decrease substantially after the addition of the catalyst. The lowest dehydrogenation temperatures of MgH_2–$x$wt.%Ni@CNT (x=2.5, 5, 7.5) are reduced by 91, 176, and 48 K. The peak hydrogen

Table 1 Comparison of hydrolysis property of Mg-based materials

Material	E_{ab}/(kJ·mol^{-1})	E_{de}/(kJ·mol^{-1})	Dehydrogenation starting temperature/°C	Source
MgH_2−5wt.%Ni@CNT	45	88	230	This work
MgH_2−Ni_3S_2@C−4	40	115	241	Ref. [12]
MgH_2−Co@CNT	−	130	268	Ref. [14]
$Mg_{0.93}Al_{0.07}$−5wt.%LaF_3	65	78	−	Ref. [37]
MgH_2−10wt.%V_2C	−	112	225	Ref. [38]
MgH_2−10wt.%CoB/CNT	−	89	240	Ref. [39]
MgH_2−10wt.%TiFe	57	113	180	Ref. [40]

emission temperature corresponding to MgH_2−5wt.%Ni@CNT is 563 K, which is considerably lower than that of pure MgH_2. The small platforms in the TPD curve are a result of uneven distribution of particles. These results indicate that the hydrogen absorption and desorption kinetics of MgH_2 can be effectively improved by the addition of Ni@CNT.

To investigate the role of the catalyst in enhancing the kinetics properties of MgH_2, the microstructures were characterized via SEM. Figures 9(a–c) display the particle morphologies of the composite during ball milling, dehydrogenation, and rehydrogenation. The size of the large particle is approximately 2−3 μm, and some small particles are uniformly dispersed around the large particle after careful observation. Figures 9(d−f) reveal the elemental mappings of MgH_2−5wt.%Ni@CNT after ball milling. The elemental mappings demonstrate excellent coincidence of C, Mg, and Ni. This result reveals that Ni@CNT particles are broken into smaller-sized particles [27], indicating that the small particles are Ni@CNT, and they are equally scattered on the surface of MgH_2 in the SEM images. However, MgH_2−5wt.%Ni@CNT exhibits no change in microscopic morphology or particle size after dehydrogenation and rehydrogenation reactions. Figures S4 and S5 (in SI) reveal that the microstructure of MgH_2−2.5wt.%Ni@CNT and MgH_2−7.5wt.%Ni@CNT in the cyclic process is similar to the conclusions above. XRD and SEM of the composites reveal that the catalyst experiences no variation in the physical phase during ball milling. The Ni particles are uniformly distributed on the surface of MgH_2 with the help of carbon materials, which can more effectively exert the catalytic effect. In addition, the carbon material attenuates the aggregation of hydrogen storage material during ball milling, hydrogen absorption, and release. The above data indicate that the presence of Mg_2Ni/Mg_2NiH_4 and CNTs provides more active sites and hydrogen diffusion channels for the whole system.

The kinetic isotherm curves reveal the improved kinetic properties of MgH_2. To investigate the impact of the catalyst on the thermodynamic performance of MgH_2, PCT measurements were applied at 623, 648, and 673 K (Fig. 10(a)). The different platforms represent the phase change of Mg/MgH_2 [41]. The values of the platform pressure of hydrogenation at 623, 648, and 673 K are 0.605, 0.988, and 1.757 MPa, respectively. The hydrogen desorption values are 0.462, 0.784, and 1.320 MPa

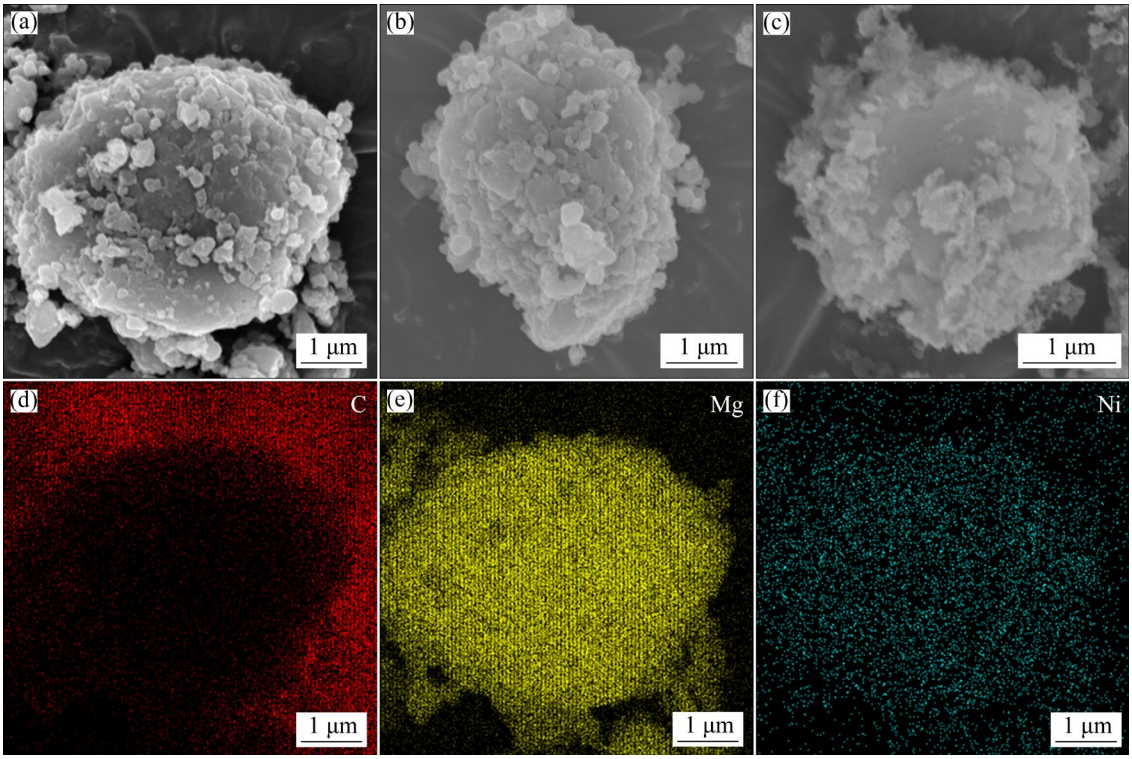

Fig. 9 SEM images of MgH_2−5.0wt.%Ni@CNT in different conditions of ball-milled (a), dehydrogenated (b) and rehydrogenated (c); Element mappings of ball-milled MgH_2−5.0wt%Ni@CNT (d−f)

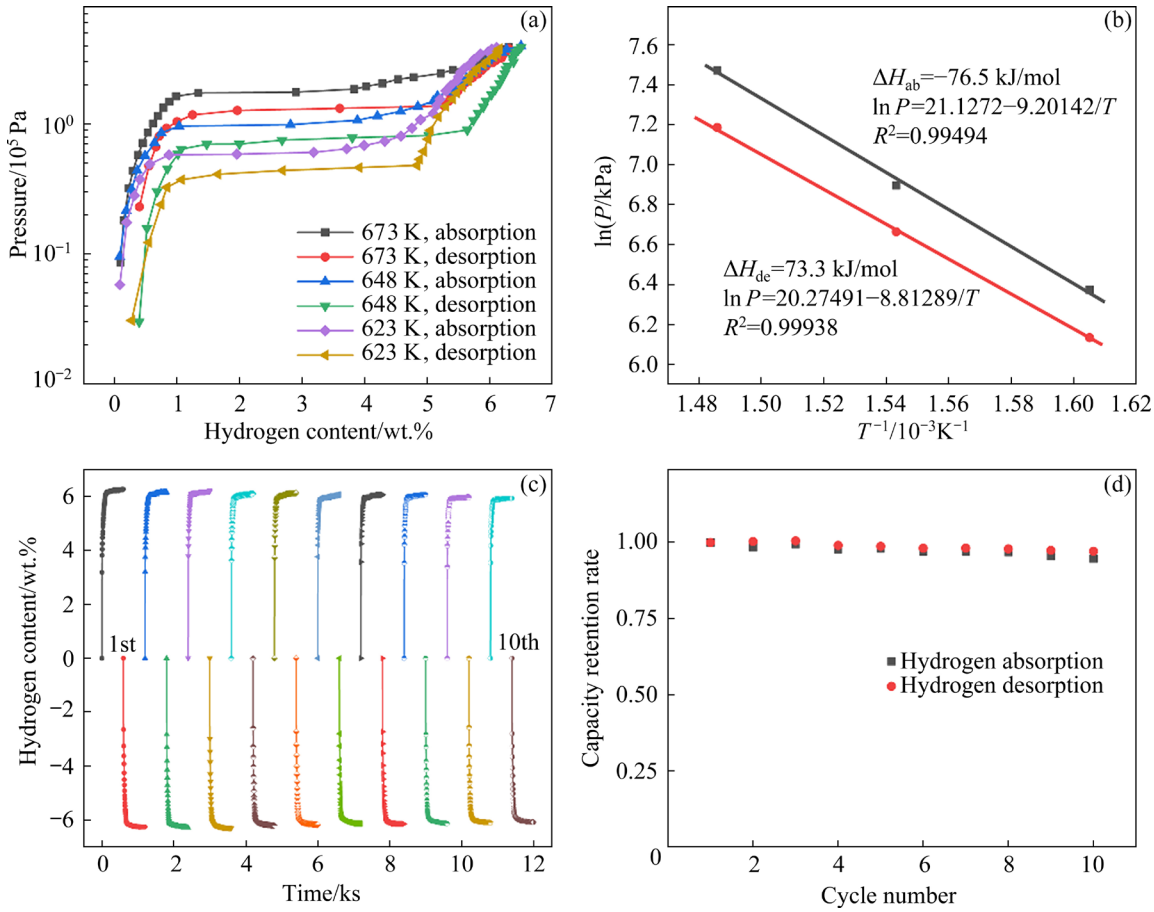

Fig. 10 PCT curves (a), Van't Hoff plots (b), cycling stability (c) and capacity retention rate (d) of MgH_2−5.0wt.%Ni@CNT composite

at 623, 648, and 673 K, respectively. According to the data measured by PCT, the enthalpy of the composites can be calculated using the Van't Hoff formula. Through calculation, the fitting formula of the hydriding composite is obtained as $\ln P = 21.1272 - 9.2014/T$, R^2 is 0.99494, the enthalpy (ΔH) is −76.5 kJ/mol, and the results are shown in Fig. 10(b). The fitted formula of the dehydriding composite is $\ln P = 20.27491 - 8.81289/T$ with a linear fit of 0.99938; the enthalpy is 73.3 kJ/mol. The enthalpy obtained in this experiment is close to that of pure MgH_2 (−75.7 kJ/mol (H_2)). The enthalpy of hydrogen release for MgH_2−7wt.%nano-VH_x sample was 74.0 kJ/mol H_2, which was experimentally obtained by ZHANG et al [42]. MENG et al [43] introduced $V_4Nb_{18}O_{55}$ as a catalyst to MgH_2 and obtained result similar to that of the present work with an enthalpy change of 75.4 kJ/mol (H_2). Thus, the addition of catalyst does not affect the thermodynamic properties of MgH_2. Recent studies have shown that reducing the size of Mg-based hydrogen storage materials can improve the thermodynamic properties. MgH_2 with a size of approximately 4−5 nm was prepared via ultrasonic solid-phase complexation following the work of ZHANG et al [44]. Notably, the enthalpy change of dehydrogenation was reduced by 22% (59.5 kJ/mol (H_2)). This result is not an exception as nanoconfinement approaches can also improve thermodynamic properties. MA et al [45] used CoS nanoboxes as a confining material to reduce the enthalpy change of hydrogen absorption and dehydrogenation of the composite to 65.6 and 68.1 kJ/mol (H_2), respectively. The thermodynamic instability is mainly attributed to the "nano-size effect" of nanoconfined Mg/MgH_2 crystals. To gain further insights into the cyclic stability of the optimal sample, the 10 cycle performances of de/hydrogenation at 673 K under 5.0 and −0.0001 MPa H_2 pressure were tested. As shown in Figs. 10(c, d), the hydrogen retention and absorption rates of the optimal sample are 97% and 95% after 10 cycles, respectively, representing its excellent cycle stability.

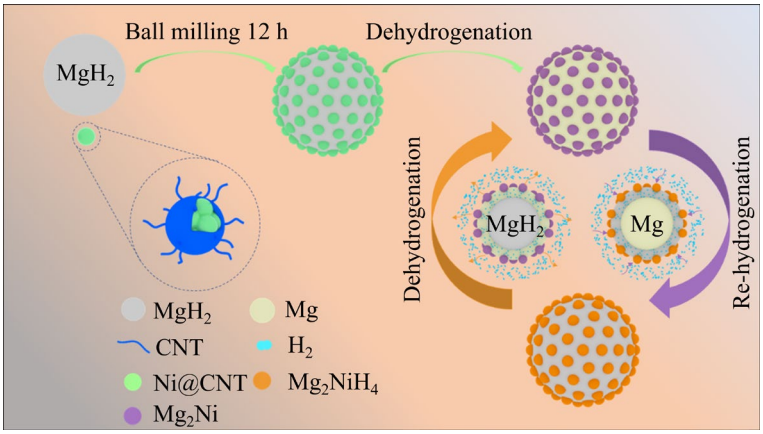

Fig. 11 Schematic illustration of catalytic mechanism of Ni@CNT composite

The schematic diagram in Fig. 11 is derived from XRD, SEM, TEM, and performance testing of the MgH_2–Ni@CNT system. The catalytic mechanisms of Ni@CNT are as follows: Firstly, the Ni@CNT catalyst is added to MgH_2 by ball milling. During the ball-milling process, the collision of stainless steel pellets cause Ni@CNT to break and distribute evenly around MgH_2. Secondly, along with the conversion of MgH_2 into Mg via the initial dehydrogenation, parts of Ni and Mg in-situ generate Mg_2Ni. Lastly, Mg_2Ni is converted to Mg_2NiH_4 after hydrogen absorption. In this work, Mg_2Ni and Mg_2NiH_4 serve as a "hydrogen pump". The weak volume expansion and contraction effects caused by the Mg_2Ni/Mg_2NiH_4 phase transition near the Mg nucleus can provide diffusion paths and increase the diffusion rate of hydrogen atoms [46,47]. The broken CNT also provides more diffusion channels for H_2 and prevents the agglomeration of particles [48]. Therefore, the multiphase MgH_2–Ni@CNT composite system with multiphase grain boundaries can enhance hydrogen absorption and desorption kinetics by providing sufficient active catalytic sites and uninterrupted channels to accelerate hydrogen diffusion.

4 Conclusions

(1) The addition of Ni@CNT considerably improves the hydrogen storage property of pure MgH_2.

(2) MgH_2−5wt.%Ni@CNT exhibits the best kinetic performance. The hydrogen absorption capacity of the MgH_2−5wt.%Ni@CNT composite rapidly reaches 5.2 wt.% within 200 s at 423 K and the dehydrogenation capacity reaches 3.75 wt.% within 1000 s at 573 K.

(3) The in-suit generated Mg_2Ni and Mg_2NiH_4 act as a "hydrogen pump", providing more diffusion channels and shortening the hydrogen diffusion distance in the cycle.

(4) The presence of CNT protects the Ni particles from oxidation and agglomeration. In addition, under the action of ball milling, the broken CNTs attach to the outer layer of MgH_2, providing more active sites while reducing the agglomeration of Mg during the cycling process.

CRediT authorship contribution statement

Zi-yin DAI: Conceptualization, Methodology, Formal analysis, Software, Writing − Original draft; **Bing ZHANG:** Conceptualization, Methodology, Investigation, Software, Writing − Original draft; **Hideo KIMURA:** Visualization, Investigation; **Li-rong XIAO:** Visualization, Investigation; **Rong-han LIU:** Resources, Supervision; **Cui NI:** Software, Validation; **Chuan-xin HOU:** Supervision; **Xue-qin SUN:** Visualization; **Yu-ping ZHANG:** Investigation; **Xiao-yang YANG:** Investigation; **Rong-hai YU:** Visualization; **Wei DU:** Conceptualization, Funding acquisition, Resources, Supervision, Writing − Review & editing; **Xiu-bo XIE:** Conceptualization, Methodology, Funding acquisition, Resources, Supervision, Writing − Review & editing.

Declaration of competing interest

The authors declare that they have no known competing financial interests or personal relationships that could have appeared to influence the work reported in this paper.

Acknowledgments

This work was supported by the National Natural Science Foundation of China (Nos. 52101274, 51731002), Natural Science Foundation of Shandong Province, China (Nos. ZR2020QE011, ZR2022ME089), Youth Top Talent Foundation of Yantai University, China (No. 2219008), and Graduate Innovation Foundation of Yantai University, China (No. GIFYTU2240).

Supplementary Information

Supplementary Information in this paper can be found at: http://tnmsc.csu.edu.cn/download/17-p2629-2022-1477-Supplementary_Information.pdf.

References

[1] SHAO Yu-ting, GAO Hai-guang, TANG Qin-ke, LIU Ya-na, LIU Jiang-chuan, ZHU Yun-feng, ZHANG Ji-guang, LI Li-quan, HU Xiao-hui, BA Zhi-xin. Ultra−fine TiO_2 nanoparticles supported on three-dimensionally ordered microporous structure for improving the hydrogen storage performance of MgH_2 [J]. Applied Surface Science, 2022, 585: 152561.

[2] JAIN I P. Hydrogen the fuel for 21st century [J]. International Journal of Hydrogen Energy, 2009, 34(17): 7368−7378.

[3] ZHANG Jing-jing, ZHANG Bing, XIE Xiu-bo, NI Cui, HOU Chuan-xin, SUN Xue-qin, YANG Xiao-yang, ZHANG Yu-ping, KIMURA H, DU Wei. Recent advances of nanoconfinement in Mg related hydrogen storage materials: A minor review [J]. International Journal of Minerals Metallurgy and Materials, 2023, 30(1): 14−24.

[4] ZHANG Meng, XIAO Xue-zhang, MAO Jian-feng, LAN Zhen-yun, HUANG Xu, LU Yun-hao, LUO Bo-sang, LIU Mei-jia. CHEN Man, CHEN Li-xin. Synergistic catalysis in monodispersed transition metal oxide nanoparticles anchored on amorphous carbon for excellent low-temperature dehydrogenation of magnesium hydride [J]. Materials Today Energy, 2019, 12: 146−154.

[5] ZHANG Meng, XIAO Xue-zhang, LUO Bo-sang, LIU Mei-jia. CHEN Man, CHEN Li-xin. Superior de/hydrogenation performances of MgH_2 catalyzed by 3D flower-like TiO_2@C nanostructures [J]. Journal of Energy Chemistry, 2020, 46: 191−198.

[6] ABDALLA A M, HOSSAIN S, NISFINDY O B, AZAD A T, DAWOOD M, AZAD A K. Hydrogen production, storage, transportation and key challenges with applications: A review [J]. Energy Conversion and Management, 2018, 165: 602−627.

[7] JAIN I P, LAL C, JAIN A. Hydrogen storage in Mg: A most promising material [J]. International Journal of Hydrogen Energy, 2010, 35(10): 5133−5144.

[8] ZHANG Meng, XIAO Xue-zhang, HANG Zhou-ming, CHEN Man, WANG Xuan-cheng, ZHANG Nan, CHEN Li-xin. Superior catalysis of NbN nanoparticles with intrinsic multiple valence on reversible hydrogen storage properties of magnesium hydride [J]. International Journal of Hydrogen Energy, 2021, 46(1): 814−822.

[9] EOM N, BHUIYAN M H, KIM T S, HONG S J. Synthesis and characterization of agglomerated coarse Al powders comprising nanoparticles by low energy ball milling process [J]. Materials Transactions, 2011, 52(8): 1674−1678.

[10] ZHANG Jian, HE Liu, YAO Yuan, ZHOU Xiao-jie, JIANG Li-kun, PENG Ping. Hydrogen storage properties of magnesium hydride catalyzed by Ni-based solid solutions [J]. Transactions of Nonferrous Metals Society of China, 2022, 32(2): 604−617.

[11] CHEN Yan, ZHANG Hao-yu, WU Fu-ying, SUN Ze, ZHENG Jia-guang, ZHANG Liu-ting, CHEN Li-xin. Mn nanoparticles enhanced dehydrogenation and hydrogenation kinetics of MgH_2 for hydrogen storage [J]. Transactions of Nonferrous Metals Society of China, 2021, 31(11): 3469−3477.

[12] ZENG Liang, LAN Zhi-qiang, LI Bao-bao, LIANG Hui-ren, WEN Xiao-bin, HUANG Xian-tun, TAN Jun, LIU Hai-zhen, ZHOU Wen-zheng, GUO Jin. Facile synthesis of a Ni_3S_2@C composite using cation exchange resin as an efficient catalyst to improve the kinetic properties of MgH_2 [J]. Journal of Magnesium and Alloys, 2022, 10(12): 3628−3640.

[13] CEHN Man, XIAO Xue-zhang, ZHANG Meng, MAO Jian-feng, ZHENG Jia-guang, LIU Mei-jia, WANG Xuan-cheng, CEHN Li-xin. Insights into 2D graphene-like TiO_2 (B) nanosheets as highly efficient catalyst for improved low-temperature hydrogen storage properties of MgH_2 [J]. Materials Today Energy, 2020, 16: 100411.

[14] LIU Mei-jia, XIAO Xue-zhang, ZHAO Shu-chun, SINA Saremi-Yarahmadi, CEHN Man, ZHENG Jia-guang, LI Shou-quan, CEHN Li-xin. ZIF-67 derived Co@CNTs nanoparticles: Remarkably improved hydrogen storage properties of MgH_2 and synergetic catalysis mechanism [J]. International Journal of Hydrogen Energy, 2019, 44(2): 1059−1069.

[15] ZHOU Xiao-cao, ZHAO Hai-bo, FU Zhi-bing, QU Jing, ZHONG Ming-long, YANG Xi, YI Yong, WANG Chao-yang. Nanoporous Ni with high surface area for potential hydrogen storage application [J]. Nanomaterials (Basel), 2018, 8(6): 394.

[16] YANG Xing-lin, HOU Quan-hui, YU Li-bing, ZHANG Jia-qi. Improvement of the hydrogen storage characteristics of MgH_2 with a flake Ni nano-catalyst composite [J]. Dalton Transactions, 2021, 50(5): 1797−1807.

[17] GAO Hai-guang, SHI Rui, SHAO Yu-ting, LIU Ya-na, ZHU Yun-feng, ZHANG Ji-guang, LI Li-quan. Catalysis derived from flower-like Ni MOF towards the hydrogen storage performance of magnesium hydride [J]. International Journal of Hydrogen Energy, 2022, 47(15): 9346−9356.

[18] HUANG Tian-ping, HUANG Xu, HU Chuan-zhu, WANG Jie, LIU Hua-bing, XU Hao, SUN Feng-zhan, MA Zhe-wen, ZOU Jian-xin, DING Wen-jiang. MOF-derived Ni nanoparticles dispersed on monolayer MXene as catalyst for improved hydrogen storage kinetics of MgH_2 [J]. Chemical Engineering Journal, 2021, 421: 127851.

[19] LAN Zhi-qiang, ZENG Liang, JIONG Guo, HUANG Xian-tun, LIU Hai-zhen, HUA Ning, GUO Jin. Synthetical

catalysis of nickel and graphene on enhanced hydrogen storage properties of magnesium [J]. International Journal of Hydrogen Energy, 2019, 44(45): 24849−24855.

[20] YAO Peng-yang, JIANG Ying, LIU Yang, WU Cheng-zhang, CHOU K C, LYU T, LI Qian. Catalytic effect of Ni@rGO on the hydrogen storage properties of MgH_2 [J]. Journal of Magnesium and Alloys, 2020, 8(2): 461−471.

[21] REYHANI A, MORTAZAVI S Z, MIRERSHADI S, MOSHFEGH A Z, PARVIN P, GOLIKAND A N. Hydrogen storage in decorated multiwalled carbon nanotubes by Ca, Co, Fe, Ni, and Pd nanoparticles under ambient conditions [J]. Journal of Physical Chemistry C, 2011, 115(14): 6994−7001.

[22] SUN Yan-yan, LI Xue-wen, CAI Zhong-shun, BAI Hong-zhen, TANG Gu-ping, HOU Zhao-yin. Synthesis of 3D N-doped graphene/carbon nanotube hybrids with encapsulated Ni NPs and their catalytic application in the hydrogenation of nitroarenes [J]. Catalysis Science & Technology, 2018, 8(19): 4858−4863.

[23] REN Li, ZHU Wen, ZHANG Qiu-yu, LU Chong, SUN Feng-zhan, LIN Xi, ZOU Jian-xin. MgH_2 confinement in MOF-derived N-doped porous carbon nanofibers for enhanced hydrogen storage [J]. Chemical Engineering Journal, 2022, 434: 134701.

[24] ZHOU Chun-yu, SZPUNAR J A, CUI Xiao-yu. Synthesis of Ni/graphene nanocomposite for hydrogen storage [J]. ACS Applied Materials & Interfaces, 2016, 8(24): 15232−15241.

[25] GONÇALVES L P L, MELEDINA M, MELEDIN A, PETROVYKH D Y, SOUSA J P S, SOARES O S G P, KOLEN'KO Y V, PEREIRA M F R. Understanding the importance of N-doping for CNT-supported Ni catalysts for CO_2 methanation [J]. Carbon, 2022, 195: 35−43.

[26] WU Hao, HUANG Fang-zhi, WANG Bao-jun, WANG Shi-peng, NIE Wen-bo, LI Shi-kuo, LIU Feng-hua, ZHANG Hui. Decorating CoNi alloy-encapsulated carbon nanotube hollow nanocages to enable dielectric loss for highly efficient microwave absorption [J]. ACS Applied Nano Materials, 2022, 5(9): 13187−13197.

[27] ZHANG Bing, XIE Xiu-bo, WANG Yu-kun, HOU Chuan-xin, SUN Xue-qin, ZHANG Yu-ping, YANG Xiao-yang, YU Rong-hai, DU Wei. In situ formation of multiple catalysts for enhancing the hydrogen storage of MgH_2 by adding porous $Ni_3ZnC_{0.7}$/Ni loaded carbon nanotubes microspheres [J]. Journal of Magnesium and Alloys, 2024, 12(3): 1227−1238.

[28] YAO Yun-jin, ZHANG Jie, WU Guo-dong, WANG Shao-bin, HU Yi, SU Cong, XU Tong-wen. Iron encapsulated in 3D N−doped carbon nanotube/porous carbon hybrid from waste biomass for enhanced oxidative activity [J]. Environmental Science and Pollution Research, 2017, 24(8): 7679−7692.

[29] YANG Huan-huan, NIE Ren-feng, XIA Wang, YU Xiao-long, JIN Ding-feng, LU Xin-huan, ZHOU Dan, XIA Qing-hua. Co embedded within biomass-derived mesoporous N-doped carbon as an acid-resistant and chemo selective catalyst for transfer hydrodeoxygenation of biomass with formic acid [J]. Green Chemistry, 2017, 19(23): 5714−5722.

[30] XIE Xiu-bo, ZHANG Bing, KIMURA H, NI Cui, YU Rong-hai, DU Wei. Morphology evolution of bimetallic Ni/Zn−MOFs and derived $Ni_3ZnC_{0.7}$/Ni/ZnO used to destabilize MgH_2 [J]. Chemical Engineering Journal, 2023, 464: 142630.

[31] LI Xin-jun, FU Yao-kun, XIE Yi-chao, CONG Lian, YU Han, ZHANG Lu, LI Yuan, HAN Shu-min. Effect of Ni/tubular g-C_3N_4 on hydrogen storage properties of MgH_2 [J]. International Journal of Hydrogen Energy, 2021, 46(66): 33186−33196.

[32] AN Cui-hua, DENG Qi-bo. Improvement of hydrogen desorption characteristics of MgH_2 with core−shell Ni@C composites [J]. Molecules, 2018, 23(12): 3113.

[33] ZHANG Jia-qi, HOU Quan-hui, GUO Xin-tao, YANG Xing-lin. Achieve high-efficiency hydrogen storage of MgH_2 catalyzed by nanosheets $CoMoO_4$ and rGO [J]. Journal of Alloys and Compounds, 2022, 911: 165153.

[34] DAN Liang, WANG Hui, LIU Jiang-wen, OUYANG Liu-zhang, ZHU Min. H_2 plasma reducing Ni nanoparticles for superior catalysis on hydrogen sorption of MgH_2 [J]. ACS Applied Energy Materials, 2022, 5(4): 4976−4984.

[35] KISSINGER H E. Reaction kinetics in differential thermal analysis [J]. Analytical Chemistry, 1957, 29: 1702−1706.

[36] ZALUSKA A, ZALUSKI L, STRÖM-OLSEN J O. Nanocrystalline magnesium for hydrogen storage [J]. Journal of Alloys and Compounds, 1999, 288: 217−225.

[37] ZHONG Hai-chang, LIN Chen-long, DU Zi-yu, CAO Chun-yan, LIANG Chu, ZHENG Qing-rong, DAI Le-yang. Hydrogen storage properties of Mg (Al) solid solution alloy doped with LaF_3 by ball milling [J]. Transactions of Nonferrous Metals Society of China, 2022, 32(6): 1969−1980.

[38] LU Cheng-lin, LIU Hai-zhen, XU Li, LUO Hui, HE Shi-xuan, DUAN Xing-qing, HUANG Xian-tun, WANG Xin-hua, LAN Zhi-qiang, GUO Jin. Two-dimensional vanadium carbide for simultaneously tailoring the hydrogen sorption thermodynamics and kinetics of magnesium hydride [J]. Journal of Magnesium and Alloys, 2022, 10(4): 1051−1065.

[39] GAO Shi-chao, LIU Hai-zhen, XU Li, LI Shou-quan, WANG Xin-hua, YAN Mi. Hydrogen storage properties of nano-CoB/CNTs catalyzed MgH_2 [J]. Journal of Alloys and Compounds, 2018, 735: 635−642.

[40] LU Xiong, ZHANG Liu-ting, YU Hai-jie, LU Zhi-yu, HE Jia-huan, ZHENG Jia-guang, WU Fu-ying, CHEN Li-xin. Achieving superior hydrogen storage properties of MgH_2 by the effect of TiFe and carbon nanotubes [J]. Chemical Engineering Journal, 2021, 422: 130101.

[41] LU Zhi-yu, YU Hai-jie, LU Xiong, SONG Meng-chen, WU Fu-ying, ZHENG Jia-guang, YUAN Zhi-fei, ZHANG Liu-ting. Two-dimensional vanadium nanosheets as a remarkably effective catalyst for hydrogen storage in MgH_2 [J]. Rare Metals, 2021, 40(11): 3195−3204.

[42] ZHANG Xue-lian, ZHANG Xin, ZHANG Ling-chao, HUANG Zhen-guo, FANG Fang, YANG Ya-xiong, GAO Ming-xia, PAN Hong-ge, LIU Yong-feng. Remarkable low−temperature hydrogen cycling kinetics of Mg enabled by VH nanoparticles [J]. Journal of Materials Science & Technology, 2023, 144: 168−177.

[43] MENG Yang, JU Shun-long, CHEN Wei, CHEN Xiao-wei, XIA Guang-lin, SUN Da-lin, YU Xue-bin. Design of bifunctional Nb/V interfaces for improving reversible

hydrogen storage performance of MgH_2 [J]. Small Structures, 2022, 3(10): 2200119.

[44] ZHANG Xin, LIU Yong-feng, REN Zhuang-he, ZHANG Xue-lian, HU Jian-jiang, HUANG Zhen-guo, LU Yun-hao, GAO Ming-xia, PAN Hong-ge. Realizing 6.7 wt.% reversible storage of hydrogen at ambient temperature with non-confined ultrafine magnesium hydrides [J]. Energy & Environmental Science, 2021, 14(4): 2302−2313.

[45] MA Zhe-wen, PANDA S, ZHANG Qiu-yu, SUN Feng-zhan, KHANA D, DING Wen-jiang, ZOU Jian-xin. Improving hydrogen sorption performances of MgH_2 through nanoconfinement in a mesoporous CoS nano-boxes scaffold [J]. Chemical Engineering Journal, 2021, 406: 126790.

[46] LI Guang-xu, LAN Zhi-qiang, TSENG Yu-sheng, ZHOU Wen-zheng, GUO Jin, CHAN S L I. Penetration and diffusion of hydrogen in Mg_2Ni: A first-principles investigation [J]. International Journal of Hydrogen Energy, 2017, 42(5): 3097−3105.

[47] CERMARK J, DAVID B. Catalytic effect of Ni, Mg_2Ni and Mg_2NiH_4 upon hydrogen desorption from MgH_2 [J]. International Journal of Hydrogen Energy, 2011, 36(21): 13614−13620.

[48] GAO Shi-chao, WANG Xin-hua, LIU Hai-zhen, HE Ting, LI Shou-quan, YAN Mi. The dehydrogenation mechanism and cycling property of MgH_2 modified by CoB/CNTs addition [J]. Chemistryselect, 2019, 4(34): 9934−9939.

一步煅烧 Ni-MOF 前驱体合成具有蠕虫状结构的 Ni@CNT 以提高 MgH_2 的储氢性能

代子寅[1]，张 冰[1]，Hideo KIMURA[1]，肖立嵘[1]，刘容含[1]，倪 翠[1]，
侯传信[1]，孙学勤[1]，张玉平[1]，杨晓阳[1]，于荣海[2]，杜 伟[1]，解秀波[1]

1. 烟台大学 环境与材料工程学院，烟台 264005；
2. 北京航空航天大学 材料科学与工程学院 空天先进材料与服役教育部重点实验室，北京 100191

摘 要：将镍基金属−有机框架(MOF)前驱体通过“过滤+煅烧”的简便方法合成镍包覆的碳纳米管(Ni@CNT)复合材料，并作为 MgH_2 的催化剂使用。通过球磨将 MgH_2 与不同质量分数的 Ni@CNT (2.5%、5.0%、7.5%)均匀混合。MgH_2−5%Ni@CNT 复合材料表现出最优异的性能，423 K 温度下可以在 200 s 内吸附 5.2% (质量分数)的氢气，并且在 573 K 下 1000 s 内可以释放约 3.75% (质量分数)的氢气，复合材料的放氢和再氢化激活能分别下降到 87.63 和 45.28 kJ/mol (H_2)。原位合成的 Mg_2Ni/Mg_2NiH_4 表现出良好的催化效果，作为“氢泵”为系统提供更多的氢扩散通道。碳纳米管的存能在一定程度上提高 MgH_2 的性能。

关键词：镁基储氢材料；激活能；镍负载碳纳米管；催化剂；机理

(Edited by Bing YANG)